remote sensing

MDPI

Article

UAV-Based Estimation of the Two-Dimensional Spatial Distribution of the Refractive Index Structure Constant

Changyu Liu [1,2], Tao Luo [1,3,*], Xuebin Li [1,3] and Shumei Deng [4]

[1] Key Laboratory of Atmospheric Optics, Anhui Institute of Optics and Fine Mechanics, Hefei Institute of Physical Science (HFIPS), Chinese Academy of Sciences, Hefei 230031, China; lcysandy@mail.ustc.edu.cn (C.L.); xbli@aiofm.ac.cn (X.L.)
[2] Anhui Technical College of Industry and Economy, Hefei 230051, China
[3] Advanced Laser Technology Laboratory of Anhui Province, Hefei 230037, China
[4] Anhui Jianzhu University, Hefei 230009, China; dsm@ahjzu.edu.cn
* Correspondence: luotao@aiofm.ac.cn

Highlights

What are the main findings?

- To overcome the limitations of traditional single-point measurements, this study developed a UAV-based observation system that integrates a semi-empirical triangle method with similarity functions to retrieve the spatial distribution of atmospheric optical turbulence at an ultra-high resolution of 0.045 m. Validation against micro-thermometer observations showed good agreement (r = 0.85, $RMSE$ = 0.44).
- Because similarity-function studies over complex and heterogeneous land surfaces are still limited, we fitted local similarity functions for a rural mixed farmland–grassland surface. Compared with the traditional W73 model for turbulence estimation, the correlation coefficient increased from 0.775 to 0.863, and the RMSE decreased by 23.09%.

What are the implications of the main findings?

- The proposed UAV-based framework provides a new and practical pathway for planar-scale, high-resolution turbulence estimation, improving spatial representativeness beyond fixed-point observations.
- The results demonstrate that site-specific similarity functions can substantially improve turbulence retrieval accuracy over heterogeneous surfaces, supporting more reliable applications in near-surface atmospheric monitoring and optical propagation studies.

Abstract

The refractive index structure constant (C_n^2) is a crucial parameter for quantifying the intensity of atmospheric optical turbulence. However, directly measuring its two-dimensional (2D) spatial distribution remains a significant challenge. In this study, we propose a novel unmanned aerial vehicle (UAV)-based method to estimate the 2D spatial distribution of near-surface C_n^2. This approach integrates a semi-empirical triangular method with the Monin–Obukhov similarity theory (MOST) for the atmospheric surface layer. Utilizing the customized UAV system, we conducted flight experiments on 12 October 2024 over a heterogeneous surface of farmland and grassland in Shouxian, Anhui Province, China. A total of 144 sets of imagery with a high spatial resolution of 0.045 m were acquired to map the planar-scale C_n^2 across the study area. To improve the accuracy of model estimation, observational data were used to fit similarity functions tailored to the complex underlying surface of the study area. Compared with the traditional W73 model, the newly fitted functions improved the estimation accuracy by 8.8%. The UAV-derived estimates were validated at the pixel scale against in situ measurements from a micro-thermometer mounted

Check for updates

Academic Editor: Alexander Marshak

Received: 24 July 2026
Revised: 20 September 2026
Accepted: 4 October 2026
Published: 8 October 2026

Copyright: © 2026 by the authors. Licensee MDPI, Basel, Switzerland. This article is an open access article distributed under the terms and conditions of the Creative Commons Attribution (CC BY) license.

on a meteorological tower. The results demonstrate that the UAV estimated C_n^2 captures the diurnal variation trends of the ground-based measurements, with magnitudes ranging from 10^{-15} to 10^{-12}. Statistical analysis yields a strong correlation coefficient (r) of 0.85 and a root mean square error ($RMSE$) of 0.44. By overcoming the limitations of traditional single-point measurements, in this study, we successfully characterize high-spatial-resolution C_n^2 distributions and offers an effective technical framework for areal-scale turbulence estimation.

Keywords: unmanned aerial vehicle (UAV); two-dimensional (2D) spatial distribution; refractive index structure constant (C_n^2); Monin–Obukhov similarity theory (MOST); surface layer similarity functions

1. Introduction

Atmospheric activity in the near-surface layer is highly complex, characterized by intense energy exchange [1]. Consequently, the impact of atmospheric turbulence on beam propagation is non-negligible. The refractive index structure constant (C_n^2) is a fundamental parameter describing the atmospheric perturbation effects on light wave propagation [2,3], and is widely applied to analyze turbulence-induced degradation in optical beam transport [4]. Currently, conventional in situ measurement techniques for quantifying near-surface optical turbulence intensity are relatively mature, including the use of micro-thermometers, 3D ultrasonic anemometers, and large-aperture scintillator [5,6]. However, these traditional methods are generally limited to single-point or path-averaged observations. Although such measurements provide reliable information on the local turbulence state, their limited spatial sampling makes it difficult to resolve the spatial heterogeneity of C_n^2 over heterogeneous land surfaces. In recent years, the rapid advancement of unmanned aerial vehicle (UAV) technology characterized by flexible deployment and real-time data acquisition has led to its widespread application in atmospheric sounding and environmental monitoring [7,8]. Several studies have successfully utilized multi-rotor UAVs equipped with meteorological sensors to probe the atmospheric boundary layer [9,10]. These studies have demonstrated the feasibility of UAV platforms for acquiring high-resolution atmospheric observations and characterizing the vertical and horizontal variability of boundary-layer properties. Nevertheless, most UAV-based turbulence observations still rely on point measurements from onboard meteorological sensors or repeated sampling along flight paths, and direct retrieval of spatially continuous optical turbulence parameters remains relatively limited. In contrast, characterizing the two-dimensional (2D) spatial distribution of atmospheric optical turbulence with high spatial resolution not only reveals fine-scale turbulence structures but also comprehensively reflects the homogeneity and inhomogeneity inherent in light propagation. Consequently, this approach is of great scientific importance for assessing and mitigating optical propagation effects, as well as for improving atmospheric boundary layer modeling and forecasting.

Numerical simulation methods, statistical interpolation techniques, and inversion algorithms are commonly used to estimate the two-dimensional (2D) spatial distribution of C_n^2. Numerical simulations based on large-eddy simulation (LES) and turbulent structure functions can effectively model the distribution of C_n^2 under diverse atmospheric stratification conditions [11]. However, due to the high complexity of these models, they are heavily dependent on initial and boundary conditions, which limits their widespread application in large-scale practical measurements and validation [12,13]. Statistical interpolation methods estimate the spatial distribution over larger areas using data from a limited number of observation sites. Nevertheless, their accuracy is highly dependent on the number, spatial

distribution, and quality of the observation data. In cases of sparse observations or strong regional variability, the reliability of interpolation results may be significantly reduced [14]. Inversion algorithms estimate C_n^2 based on observational data and appropriate prior information [15]. However, under complex terrain conditions, uncertainties in prior information and the nonlinear variation in atmospheric properties may lead to poor reliability of the retrieved results. These limitations indicate that obtaining spatially continuous C_n^2 information requires an observation framework that can simultaneously retain the spatial flexibility of remote sensing and the physical interpretability of turbulence parameterization.

Unmanned aerial vehicle (UAV) technology, with its flexible observation capability and advantage of real-time data acquisition at high spatial resolution, can effectively overcome the limitations of traditional methods in spatial distribution measurements [16,17]. Recent advances in UAV-based atmospheric observation have demonstrated their potential for extending turbulence measurements from isolated points to spatially distributed observations. By integrating UAV remote sensing imagery with appropriate physical models and data processing approaches, C_n^2 can be estimated over a two-dimensional (2D) spatial domain [18]. By integrating UAV remote sensing imagery with advanced data processing algorithms and machine learning techniques, C_n^2 can be rapidly estimated on a two-dimensional (2D) spatial distribution. Therefore, UAV-mounted sensor-based measurement methods have gradually become an important approach for investigating atmospheric optical turbulence in two dimensions. This technique provides a new technological pathway for acquiring C_n^2 in complex terrain and diverse environmental conditions, while also expanding the spatial coverage of observations.

This study presents an innovative UAV-based measurement system for atmospheric optical turbulence intensity C_n^2. By integrating aerial data acquisition with a semi-empirical triangle method (SMTM) coupled with a similarity function-based estimation framework, the system enables the quantitative inversion of C_n^2 across heterogeneous underlying surfaces. This approach overcomes the limitations of traditional single-point measurements and captures the high-spatial-resolution distribution of C_n^2 on a two-dimensional spatial distribution.

2. Data and Methodology

In this study, a series of aerial survey experiments was conducted on 12 October 2024 using a multi-sensor UAV platform in Shouxian, Anhui Province, China (116°47′15″E, 32°26′9″N). The study area comprises two distinct surface types: cropland on the left and grassland on the right, separated by a paved road and a field ridge. A total of 21 flights were executed from 07:20 to 17:20 under predominantly sunny, clear, or partly cloudy weather conditions. The UAV acquired imagery while hovering at an altitude of 100 m in fixed-cruise mode, with the MicaSense Altum-PT sensor operated at a maximum trigger rate of 1 Hz. Consequently, 144 sets of image data were acquired at 10 min intervals, with each observation covering an area of approximately 8104.59 m^2. The geographical location of the study area is illustrated in Figure 1. The red rectangular outline in the enlarged inset in the upper-left corner indicates the spatial extent of the UAV imagery, while the red "Sampling Location" denotes the location of the near-surface meteorological observation tower within the UAV-mapped domain.

2.1. Experimental Platform and Instrumentation

Specifically, a DJI Matrice 350 RTK (M350) quadcopter UAV was used to conduct the flight tests (Figure 2a), while ground meteorological conditions were monitored simultaneously (Figure 2b–d). The M350 platform has a maximum payload capacity of 2.7 kg and an average flight endurance of approximately 55 min, with the actual duration depending on wind speed, humidity, and altitude. Under standard operating conditions, the UAV

has a maximum flight speed of 18 m/s and can withstand wind speeds of up to 12 m/s. Owing to its vertical takeoff and landing (VTOL) capability, the UAV is well suited for field deployment. Flight missions were pre-programmed and managed using DJI Pilot software. Reliable wireless communication among the transmitter, UAV, and ground station was established via the 2.4 GHz band.

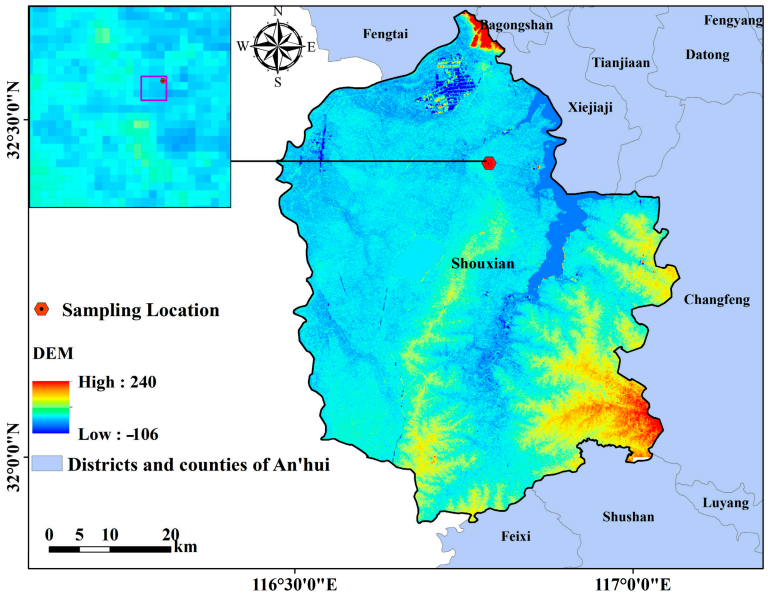


Figure 1. Location of the Shouxian Observation Station.

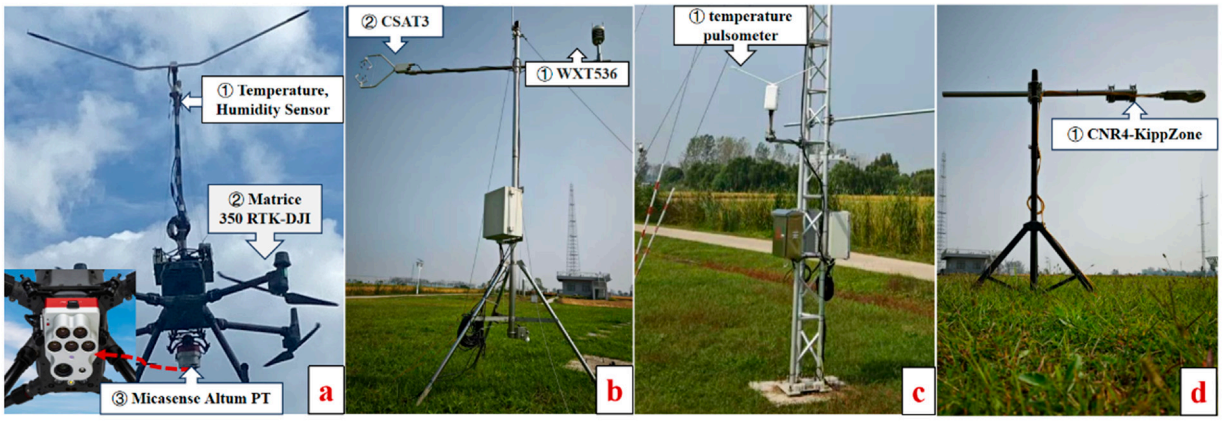


Figure 2. Observational equipment utilized in this study: (**a**) UAV platform (DJI Matrice 350 RTK) equipped with a temperature–humidity sensor and a MicaSense Altum-PT sensor; (**b**) ground meteorological instruments, including a WXT536 weather transmitter and a CSAT3 sonic anemometer; (**c**) tower-mounted temperature–humidity sensor; (**d**) CNR4 net radiometer (Kipp & Zonen).

During steady-state flight or hovering, the propellers of the M350 UAV operate at a rotational speed of approximately 5000 to 6000 rpm, with minor variations depending on the payload and ambient flight conditions. The high-speed rotation of the propellers generates a downward-propagating airflow characterized by tip vortices [19]. The intensity and spatial distribution of these vortices are modulated by the aerodynamic interactions between the thrust fields of individual rotors, resulting in localized turbulence and complex flow structures. Numerical simulations of the aerodynamic field during hovering and constant-speed flight (Figure 3) reveal that the rotor wash is predominantly directed downward, primarily perturbing the vertical wind field beneath the aircraft. Conversely, at

a distance of 1.0 m below the UAV fuselage, the disturbance induced by propeller rotation becomes negligible.

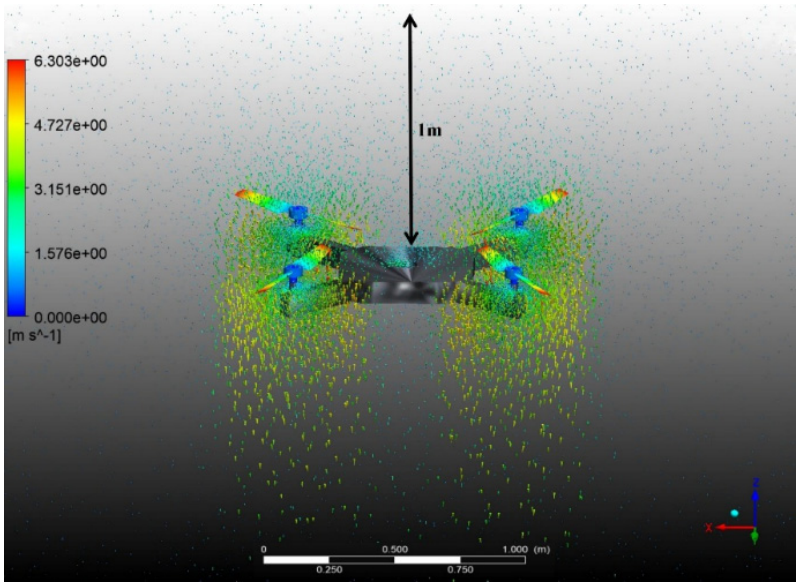


Figure 3. Simulation of the airflow field during hovering of the M350 UAV, performed using ANSYS Fluent (2025 R1) with CFD−Post post-processing for the velocity field. The simulation models the UAV hovering at 100 m above ground level in initially static ambient air, enabling the full development and dispersion of the rotor-induced downwash near the surface.

Prior to the field experiments, the rotor-induced airflow disturbance around the UAV and the resulting flow field under hovering conditions were numerically simulated at a flight altitude of 100 m. The UAV platform and onboard sensors were subsequently configured based on the simulated airflow characteristics at this altitude. To maintain consistency between the numerical simulation and the field observations, the UAV was operated at a fixed altitude of 100 m during the subsequent field experiments.

To complement UAV flight observations and validate the estimations derived from the UAV system, ground-based measurements were conducted using a suite of instruments, including a micro-thermometer, a three-dimensional ultrasonic anemometer (Model CSAT3B, Campbell Scientific, Logan, UT, USA), an automatic weather station (Model WXT536, Vaisala, Vantaa, Finland), and a four-component net radiometer (Model CNR4, Kipp & Zonen, Delft, The Netherlands). Detailed specifications, installation heights, and configurations of these ground-based sensors are summarized in Table 1.

Table 1. Summary of observation instrument parameters.

Instrument	Model	Object	Frequency	Precision	Mounting Position
Micro-thermometer	Micro	$\Delta V, \Delta T$	0.2 Hz		The peak of the observation tower is 3 m above the floor.
Three-dimensional ultrasonic anemometer	CSAT3B	$u, v, w, \mathrm{u}_*(\mathrm{m/s})$	20 Hz	±1.5%	The peak of the observation tower is 2 m above the floor.
4-component net radiometer	CNR4	$S_\downarrow, S_\uparrow, L_\downarrow, L_\uparrow$ $(\mathrm{W/m^2})$	10 Hz	±1.0%	The peak of the observation tower is 2 m above the floor.

Table 1. *Cont.*

Instrument	Model	Object	Frequency	Precision	Mounting Position
Automatic weather station	WXT536	T_a (°C) RH_a	0.2 Hz	±0.21 °C ±2.5%	The peak of the observation tower is 1 m above the floor.

The UAV-mounted MicaSense Altum-PT is an integrated 3-in-1 sensor system featuring a seven-channel camera that combines multispectral, thermal, and high-resolution panchromatic imaging. It operates in conjunction with a Downwelling Light Sensor 2 (DLS 2) and an integrated GPS module, utilizing real-time irradiance and sun-angle measurement technologies to ensure highly accurate and reliable data collection. The key specifications of the Altum-PT sensor are summarized in Table 2.

Table 2. Specifications for the Micasense Altum PT camera system.

Parameters	Micasense Altum PT
Weights	577 g
Sizes	11 × 8 × 6.9 cm
Wavelength (nm)	Blue (465 ± 32 nm), green (560 ± 27 nm), red (668 ± 14 nm), red edge (717 ± 12 nm), NIR (842 ± 57 nm), PAN, thermal infrared (7.5–13.5 um)
Resolution	2064 × 1544 (MS), 4112 × 3008 (PAN), 320 × 256 (TIR)
Focal length	55 mm
GSD at 120 m above ground	Multispectral band 0.053 m
	Thermal infrared band 0.34 m
	Panchro and Pansharped 0.025 m
Field of view	50° HFOV × 38° VFOV (MS), 46° HFOV × 35° VFOV (PAN), 48° × 39° (TIR)

To ensure radiometric accuracy, a standard calibrated reflectance panel with known spectral albedo values was imaged prior to each flight. These panel images were subsequently utilized as calibration inputs in the post-processing workflow to calibrate the multispectral imagery. The sensor also integrates a FLIR thermal infrared core supported by a built-in temperature retrieval algorithm. This algorithm employs an atmospheric radiative transfer model to calculate the atmospheric absorption and scattering of infrared radiation, thereby performing atmospheric correction. Additionally, surface temperature calibration is achieved by acquiring thermal data from reference targets with distinct reflectances to determine the corresponding radiance values. Finally, the surface emissivity is estimated using a gray-body radiation model to retrieve the final land surface temperature (LST). The thermal imagery was resampled to a spatial resolution of 0.045 m using cubic convolution interpolation, consistent with the spatial resolution of the multispectral imagery, to facilitate subsequent pixel wise calculations.

The UAV is equipped with a WSQ temperature, humidity, and pressure sensor for environmental monitoring. This high-precision, fully digital sensor integrates advanced sensing elements to enable rapid and accurate measurements of atmospheric profiles. To mitigate potential measurement interference caused by the rotor-induced downwash during flight, the sensor module is strategically mounted atop the UAV using a 1 m support rod. This mounting configuration was optimized and validated through comprehensive airflow simulations. The technical specifications of the sensor are detailed in Table 3.

Table 3. WSQ temperature, humidity, and pressure sensor measurement parameters s.

Parameter	Temperature	Humidity	Pressure
Measurement Range	−40~80 °C	0~100% RH	10~1100 hPa
Accuracy	±0.3 °C	±3% RH	±3 hPa
Resolution	0.1 °C	0.1% RH	0.1 hPa

2.2. Method

In this study, near-surface turbulence parameters, including friction velocity (u_*), temperature scale (T_*), and atmospheric stability parameter ($\xi = z/L$), were derived from the three-dimensional wind-speed components, ultrasonic virtual temperature, and other auxiliary variables measured by a three-dimensional ultrasonic anemometer [20]. To improve the estimation accuracy of the near-surface atmospheric refractive-index structure constant (C_n^2), a functional relationship between the temperature structure constant (C_T^2) and the stability parameter ($\xi = z/L$) was established for the study area based on Monin–Obukhov similarity theory (MOST). Subsequently, two-dimensional sensible heat fluxes estimated from UAV-based remote sensing data using the semi-empirical triangle method, SMTM [21], were combined with the fitted similarity function to derive the spatial distribution of C_T^2. The corresponding two-dimensional distribution of C_n^2 was then obtained using the conversion relationship between C_T^2 and C_n^2. Based on this approach, C_T^2 was estimated at multiple times during the day, allowing its diurnal variation to be analyzed in detail. The estimated results were further validated against in situ measurements obtained from a micro-thermometer. The overall methodological framework is illustrated in Figure 4.

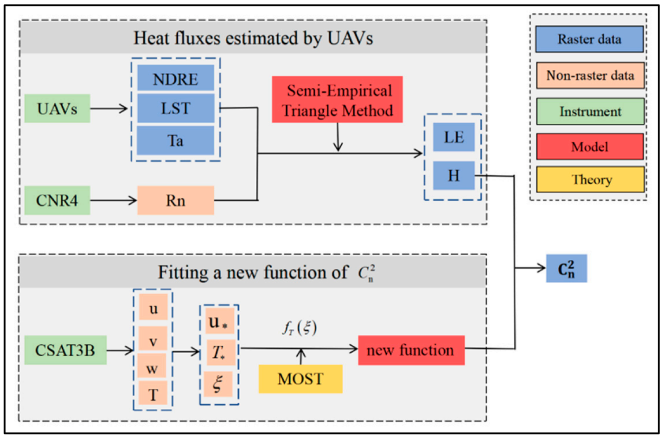


Figure 4. Research methodology.

To ensure consistency between the UAV-derived estimates and the micro-thermometer observations, both datasets were matched in terms of temporal and spatial scales. The UAV-derived C_n^2 estimates had a temporal resolution of 10 min, and the high-frequency micro-thermometer observations were averaged over the corresponding 10 min intervals for comparison. For spatial matching, the meteorological observation tower was located within the UAV-mapped domain, as indicated by the red "Sampling Location" in Figure 1. Considering the point-scale nature of the micro-thermometer measurements, a circular area with a radius of 0.5 m centered on the observation-tower location was defined. The UAV-derived C_n^2 values within this area were extracted and averaged to obtain a representative local UAV-derived C_n^2 value for comparison with the corresponding point-scale measurement from the micro-thermometer. This local spatial averaging was used to reduce the influence of individual-pixel variability while retaining the spatial information around the observation tower. Therefore, the validation was performed by comparing the

locally averaged UAV-derived C_n^2 with the corresponding point-scale micro-thermometer measurement at the same observation time.

2.2.1. Parameterized Model for Estimating C_n^2 in the Near-Surface Layer

Monin–Obukhov similarity theory (MOST) uses the stability parameter ξ to characterize near-surface atmospheric stability and to establish universal relationships between turbulent statistics, such as wind-speed and temperature gradients, and characteristic turbulent scales, such as friction velocity u_* and temperature scale T_*. Moreover, an empirical relationship between the stability parameter ξ and the atmospheric temperature structure parameter C_T^2 has been reported in previous studies [22], which can be expressed as follows:

$$f_T(\xi) = \frac{C_T^2 z^{2/3}}{T_*^2} = \frac{C_T^2 z^{2/3} u_*^2}{\overline{w'T'}^2} \tag{1}$$

In the equation, $f_T(\xi)$ is a dimensionless temperature similarity function that depends on the atmospheric stability parameter ξ. When $\xi < 0$, the atmosphere is unstable; when $\xi > 0$, the atmosphere is stable; and when $\xi = 0$, neutral stratification is indicated. The function can be expressed as follows:

$$\xi = \frac{z}{L} = \frac{zkgT_*}{u_*^2 \overline{T}} = -\frac{zkg\overline{w'T'}}{u_*^3 \overline{T}} \tag{2}$$

In the equation, L denotes the Monin–Obukhov length [23], and z is the measurement height. T' represents the temperature fluctuation, while w' denotes the fluctuation of the vertical wind-speed component. k is the von Kármán constant, which is set to 0.4 in this study; g is the gravitational acceleration; and $\overline{T}$ is the mean temperature for each sampling interval. The friction velocity u_* is calculated as follows:

$$u_* = \left[\overline{u'w'}^2 + \overline{v'w'}^2\right]^{1/4} \tag{3}$$

In addition, the temperature characteristic parameter T_* is shown below:

$$T_* = \frac{\overline{w'T'}}{u_*} \tag{4}$$

According to Monin–Obukhov similarity theory (MOST), the prediction accuracy of the near-surface parameterization C_T^2 depends, to some extent, on the similarity function $f_T(\xi)$. Therefore, establishing a predictive model for $f_T(\xi)$ that is applicable to the study area is an important approach for improving the estimation accuracy of C_T^2. Numerous studies have investigated the modeling of the similarity function $f_T(\xi)$, among which the formulation proposed by Wyngaard in 1973, hereafter referred to as W73 [24], is one of the most widely used. The expression is given as follows:

$$f_T(\xi) = \begin{cases} 4.7(1-7\xi)^{-2/3} & \xi < 0 \\ 4.9\left(1 + 2.4\xi^{2/3}\right) & \xi \geq 0 \end{cases} \tag{5}$$

As the covariance of fluctuations in atmospheric meteorological elements, turbulent heat flux is generally calculated from the covariance of the corresponding physical quantities. Specifically, the sensible heat flux (H) is derived from the covariance of vertical wind speed and temperature (Equation (6)), while the latent heat flux (LE) is computed from the covariance of vertical wind speed and specific humidity (Equation (7)).

$$H = \rho c_p \overline{w'T'} \tag{6}$$

$$LE = \rho l_v \overline{w'q'} \tag{7}$$

In the equation, ρ is the atmospheric density (kg/m^3), C_p is the specific heat capacity of dry air at constant pressure (J/(kg · K)), l_v is the latent heat of vaporization of water (J/kg), w' represents the vertical wind speed fluctuation, T' is the temperature fluctuation, and q' is the humidity fluctuation.

2.2.2. Estimation of Sensible and Latent Heat Fluxes Using the Semi-Empirical Triangle Method

In this study, turbulent heat fluxes were estimated using the semi-empirical triangle method (SMTM) [25–27], which utilizes high-resolution imagery acquired by unmanned aerial vehicles (UAVs). The SMTM is based on the empirical relationship between land surface temperature (LST) and the Normalized Difference Red Edge Index ($NDRE$). Within the SMTM framework, the Priestley–Taylor coefficient φ is parameterized, whereas the aerodynamic forcing term is expressed using a remote sensing-derived driving factor [28], computed as follows:

$$\mathrm{LE} = \left[(R_n - G)\Delta \frac{\Delta}{\Delta + \gamma} \right] \tag{8}$$

$$\mathrm{H} = R_n - G - \phi \left[(R_n - G)\Delta \frac{\Delta}{\Delta + \gamma} \right] \tag{9}$$

$$\phi = \frac{LST_{(max)} - LST_{(i)}}{LST_{(max)} - LST_{(min)}} \left[\phi_{max} - \varphi_{(i,min)} \right] + \varphi_{(i,min)} \tag{10}$$

$$\varphi_{(i,min)} = \phi_{max} \left[\frac{NDRE_{(i)} - NDRE_{(min)}}{NDRE_{(max)} - NDRE_{(min)}} \right]^2 \tag{11}$$

$$\phi_{max} = \frac{\Delta + \gamma}{\Delta} \tag{12}$$

where R_n is the net radiation measured by a CNR4 four-component radiometer, exhibiting only minor regional variations at the microscale [29]; Δ is the slope of the saturation vapor pressure curve with respect to temperature (Kpa/°C); γ is the psychrometric constant.

G is the soil heat flux, which is generally much smaller than net radiation (R_n), but it is closely related to R_n and is also influenced by vegetation conditions, particularly the normalized difference vegetation index ($NDVI$). Several empirical models with varying levels of complexity have been proposed for estimating G. In this study, the classical Bastiaanssen model (Equation (13)) and the Moran model (Equation (14)) [30,31], which requires fewer input parameters, were selected to estimate soil heat flux. The two models were comparatively validated, and the better-performing model was selected.

$$G = R_n \cdot (LST - 273.15) \cdot (0.0038 + 0.0074\alpha) \cdot (1 - NDVI^4) \tag{13}$$

$$\mathrm{G} = 0.583 \exp\left(-2.13 \mathrm{NDVI}_{(\mathrm{i})} \right) \cdot \mathrm{R_n} \tag{14}$$

As the primary parameters of the triangle method, LST and $NDRE$ were derived from the UAV aerial survey imagery.

The UAV remote sensing imagery was radiometrically calibrated using a standard reflectance calibration panel (whiteboard) and the Downwelling Light Sensor (DLS) integrated with the MicaSense Altum sensor. The DLS measurements were used to account for variations in incident illumination during image acquisition, while the onboard GPS information was used to assist in the geometric correction and spatial alignment of the imagery. These preprocessing procedures improved the consistency and comparability of

the retrieved surface reflectance. Subsequently, the calibrated red and near-infrared surface reflectance was used to calculate NDVI as [32]:

$$NDRE = \frac{B_{\mathrm{NIR}} - B_{\mathrm{RedEdge}}}{B_{\mathrm{NIR}} + B_{\mathrm{RedEdge}}} \quad (15)$$

where B_{NIR} and B_{RedEdge} represent the reflectance in the near-infrared and red-edge bands, respectively.

The calibrated images were then preprocessed using Pix4Dmapper software for orthorectification and image mosaicking, yielding the Normalized Difference Red Edge ($NDRE$) distribution map presented in Figure 5.

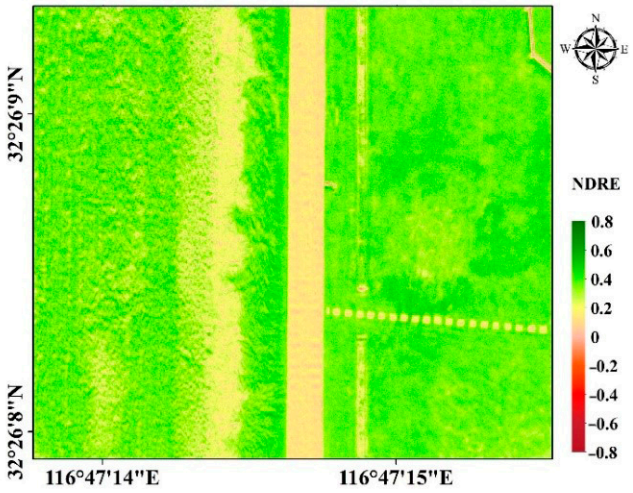


Figure 5. Spatial distribution of $NDRE$.

Land surface temperature (LST) was retrieved primarily from the FLIR thermal sensor integrated into the Altum imaging system. The digital number (DN) values from the thermal infrared band were converted to LST (°C) using a linear calibration equation [33]:

$$LST = DN \cdot 0.04 - 273.15 \quad (16)$$

Given that LST is a critical input for flux estimation, mitigating the influence of atmospheric particulates encountered during UAV flights is essential [34]. To enhance retrieval accuracy, a hot-and-cold-spot calibration method was applied to correct the retrieved temperatures. The hot−and−cold−spot correction method is based on measurements at representative "extreme cold spots" (areas with the highest vegetation cover and lowest surface temperature) and "extreme hot spots" (areas with the lowest vegetation cover and highest surface temperature). These measurements are corrected by establishing a linear relationship between the measured and inverted temperature values. In this study, an industrial hand-held thermal infrared pyrometer (ZTW0503B) was used to calibrate representative locations before and after each flight to establish their correlation, as shown in Figure 6.

Based on the linear relationship fitted in Figure 6, the land surface temperature (LST) retrieved from the UAV sensor was calibrated. The coefficient of determination (R^2) was 0.952, with a root mean square error ($RMSE$) of 0.91, a mean absolute error (MAE) of 0.725, and a relative error (RE) of 2.78%. The spatial distribution of the calibrated LST is presented in Figure 7. To clearly illustrate the local spatial details of the land surface temperature (LST) distribution, enlarged views of two rectangular regions of interest (ROIs) identified in the main LST maps are presented as circular insets below the corresponding maps for

each observation time. The two circular insets correspond to the two black rectangular boxes in the main maps, respectively, highlighting the spatial heterogeneity and local variations in LST within the selected regions. As Figure 7 shows, diurnal *LST* peaked at approximately 13:30, coinciding with the maximum solar irradiance, and declined rapidly by 17:00 (approaching sunset) as solar radiation decreased. Notably, non-vegetated areas generally exhibited higher surface temperatures than vegetated surfaces, mainly due to differences in surface thermal properties and the absence of evaporative cooling associated with vegetation.

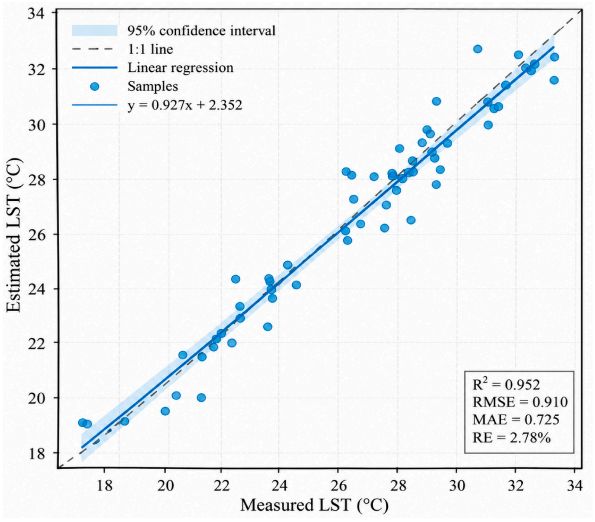


Figure 6. The land surface temperature (LST) retrieved from the thermal infrared imagery was calibrated based on a correlation analysis between the measured and retrieved LST.

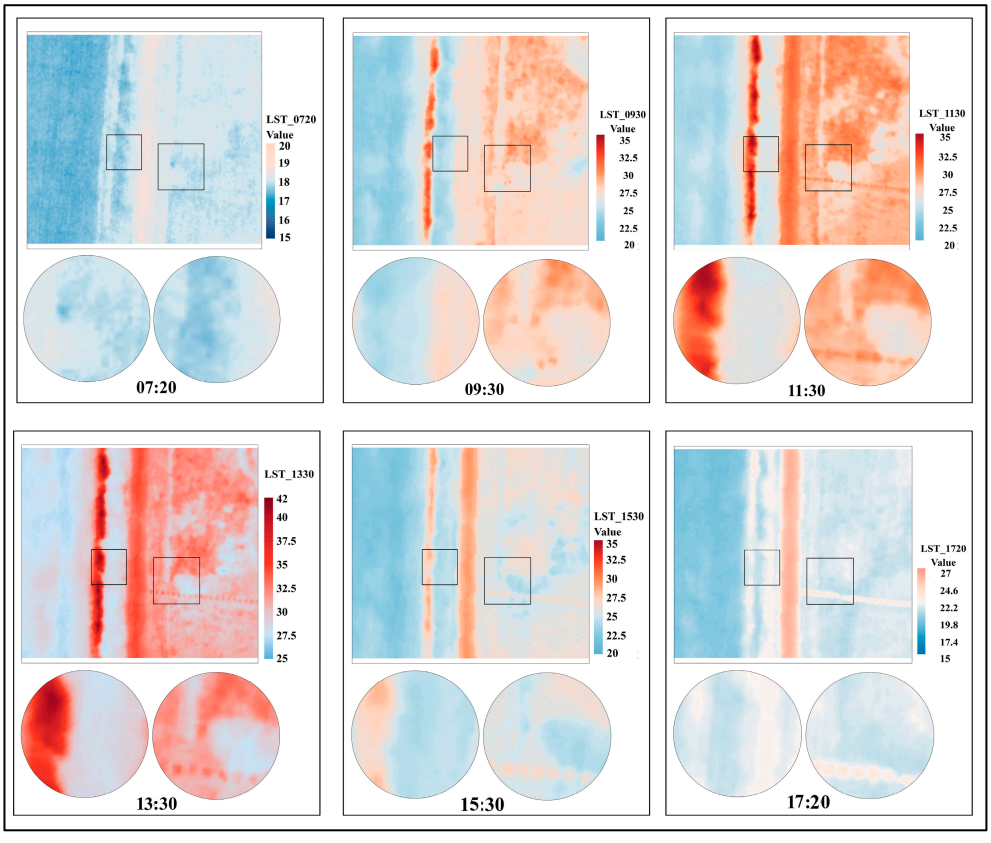


Figure 7. Temporal and spatial distribution of *LST* (°C).

2.2.3. Accuracy Assessment

To evaluate the accuracy of heat fluxes estimated from UAV remote sensing data using the semi-empirical triangle method and the refractive-index structure constant (C_n^2) combined with Monin–Obukhov similarity theory (MOST), in this study, we used the correlation coefficient (r), coefficient of determination (R^2), and root mean square error ($RMSE$), mean absolute error (MAE), and relative error (RE) as evaluation metrics. Specifically, r and R^2 were employed to characterize the correlation and linear agreement between the estimated and measured heat fluxes, while $RMSE$ and MAE quantified the absolute magnitude of the estimation errors. RE was used to assess the relative deviation of the estimated from the measured values

$$\mathrm{r} = \frac{\sum_{i=1}^{N}(X_i - \overline{X})(Y_i - \overline{Y})}{\sqrt{\sum_{i=1}^{N}(X_i - \overline{X})^2 \sum_{i=1}^{N}(Y_i - \overline{Y})^2}} \tag{17}$$

$$\mathrm{RMSE} = \sqrt{\frac{1}{N}\sum_{i=1}^{N}(Y_i - X_i)^2} \tag{18}$$

$$R^2 = 1 - \frac{\sum(X_i - Y_i)}{\sum(Y_i - \overline{Y})^2} \tag{19}$$

$$MAE = \frac{1}{N}\sum_{i=1}^{N}|Y_i - X_i| \tag{20}$$

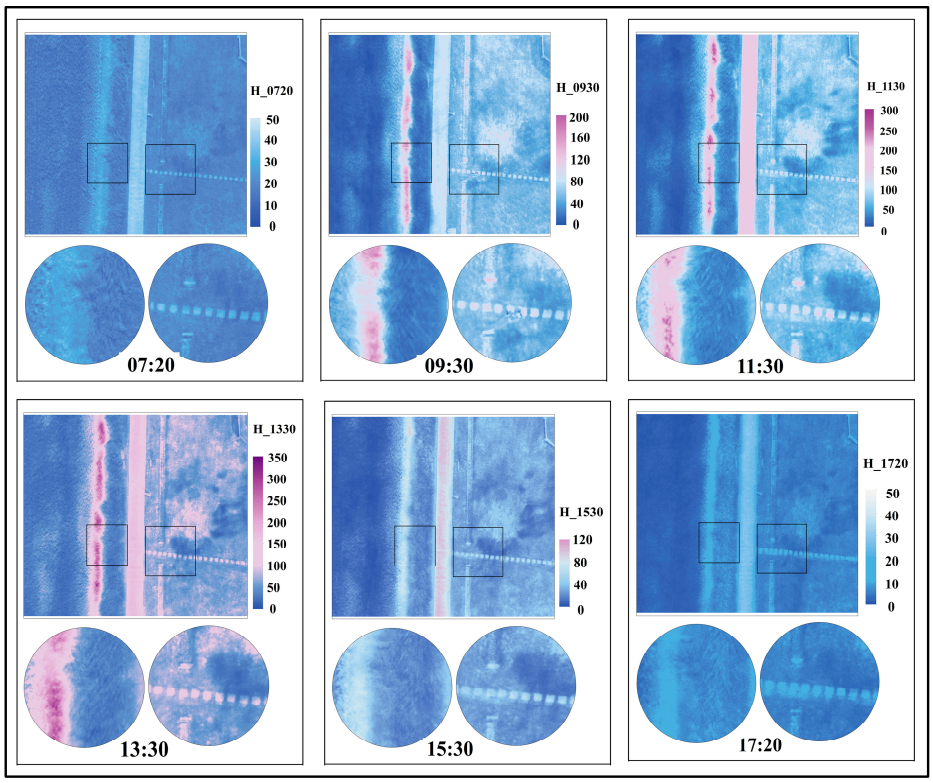
$$RE = \frac{1}{N} - \sum_{i=1}^{N}\left|\frac{Y_i - X_\mathrm{i}}{X_\mathrm{i}}\right| \times 100\% \tag{21}$$

In the equations, X_i represents the actual measured value and $\overline{X}$ represents the mean value of X_i; Y_i represents the estimated value, $\overline{Y_i}$. represents the mean value of the estimated value, and $\overline{Y}$ represents the average of the estimated values; N is the number of samples.

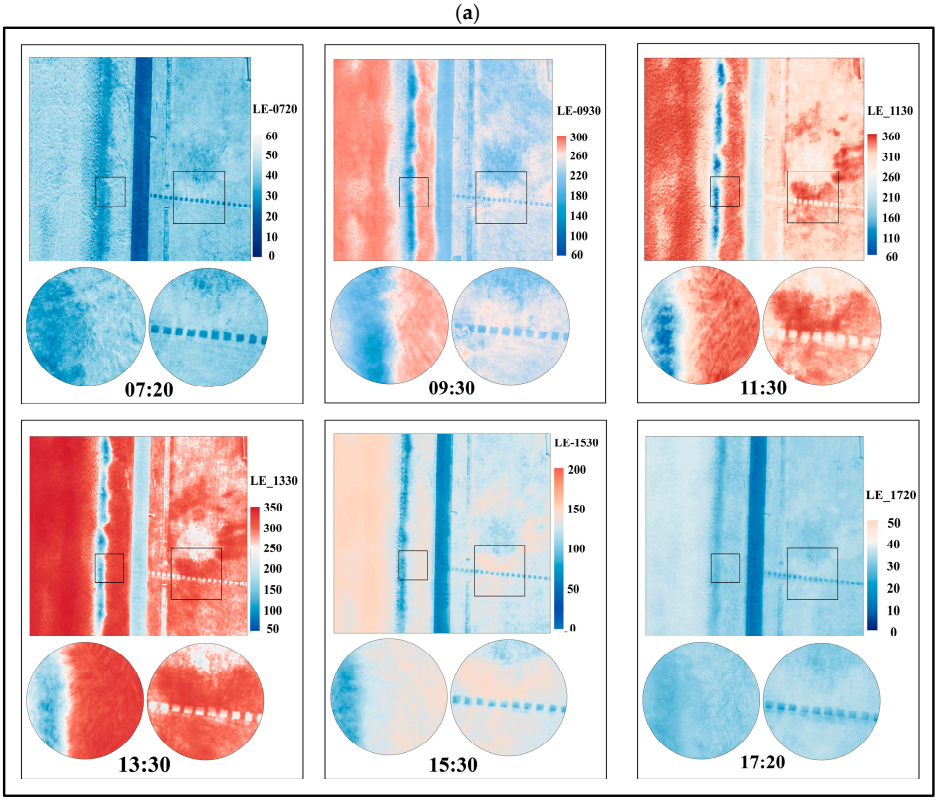
3. Results

3.1. UAV-Based Estimation and Accuracy Validation of Turbulent Heat Fluxes

Based on the LST and $NDRE$ retrieved from the UAV imagery, integrated with air temperature data collected by the onboard sensor, the sensible (H) and latent (LE) heat fluxes of the bare soil surface were estimated using Equations (8)–(13). As illustrated in Figure 8a,b, the high-spatial-resolution imagery clearly resolves the micro-scale distribution of heat fluxes. Temporally, the heat fluxes exhibited pronounced diurnal variations, peaking near solar noon and decreasing during the morning and evening. Specifically around 12:00, the rapid intensification of solar radiation triggered a sharp increase in LST, accelerating water evaporation and driving the heat fluxes to their diurnal maxima. Spatially, areas with dense vegetation cover exhibited lower sensible heat fluxes due to suppressed soil heat transfer. These vegetated regions, characterized by lower microclimate temperatures and reduced net radiation absorption, demonstrated enhanced potential evapotranspiration and higher latent heat fluxes. Conversely, artificial surfaces and terrain features (such as paved roads and field ridges) acted as radiative hot spots with concentrated heat transfer, thereby yielding elevated H and relatively lower LE.



(**a**)



(**b**)

Figure 8. (**a**) Spatial and temporal distribution of H (W/m^2) and (**b**) spatial and temporal distribution of LE (W/m^2).

The heat fluxes estimated by the UAV method showed the same diurnal pattern as those measured by the three-dimensional ultrasonic anemometer, as illustrated in Figure 9a. Both reached their maximum values between 12:00 and 12:30, during the midday period. However, because the UAV-based approach estimates the average sensible heat flux over a spatial

extent, the relatively high vegetation cover and limited surface solar radiation in the study area resulted in estimated values that were lower than the measurements obtained by the three-dimensional ultrasonic anemometer. The correlation analysis between the estimated and measured heat fluxes is presented in Figure 9b. The correlation coefficients between the UAV-derived estimates and the measured values were 0.897 for r, 0.804 for R^2, and 11.23 W/m^2 for $RMSE$, indicating a strong agreement between the two methods. During the midday period, when atmospheric turbulence is relatively strong, sensible heat flux estimated from UAV-based land surface temperature (LST) retrievals is generally lower than that derived from the eddy covariance (EC) method using a three-dimensional ultrasonic anemometer. This discrepancy is mainly due to differences in measurement scale and temporal resolution: UAV-based LST retrievals provide instantaneous surface temperature snapshots over a short period, whereas the EC method integrates high-frequency observations over time to capture turbulent heat transport. As a result, UAV-based estimates may not fully represent transient turbulent flux contributions, leading to an underestimation of H.

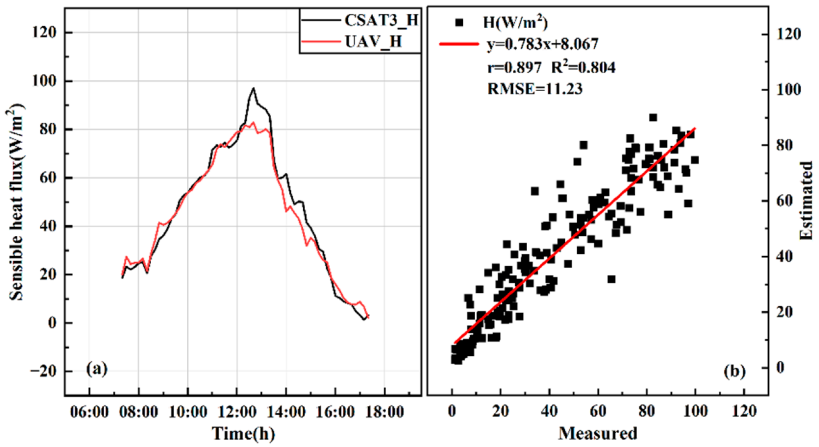


Figure 9. Comparison of UAV-estimated and observed sensible heat flux (H). (**a**) Diurnal variations in UAV-estimated and CSAT3B-observed sensible heat flux; (**b**) scatter plot of UAV-estimated versus CSAT3B-observed sensible heat flux, with the fitted regression line and statistical metrics.

Because direct field measurements of soil heat flux (G) were not available in this study, the absolute accuracy of the Moran model could not be directly evaluated against observations. To assess the consistency of different G parameterization schemes and provide a basis for model selection, G was therefore estimated using both the classical Bastiaanssen model and the Moran model based on a representative UAV image acquired at 11:30. To reduce the computational burden associated with the large number of UAV pixels, a 10 × 10 pixel spatial aggregation scheme was adopted, with every 100 pixels averaged to generate a representative G value while preserving the overall spatial variability. The aggregated G estimates from the two models were then compared at the pixel level. As shown in Figure 10, the two estimates exhibited a strong positive relationship, with R^2 of 0.814 and a Pearson correlation coefficient (r) of approximately 0.902. The corresponding RMSE and Bias were 6.285 and 5.503, respectively, indicating a high degree of consistency between the two parameterization schemes. Previous studies have also reported that the Moran model, when combined with the surface energy-balance approach, can provide turbulent heat flux estimates with an accuracy exceeding 90%. Considering the strong consistency between the Moran and Bastiaanssen estimates, the relatively small number of input parameters required by the Moran model, and its reported performance in previous studies, the Moran model was selected for G estimation in the subsequent analysis.

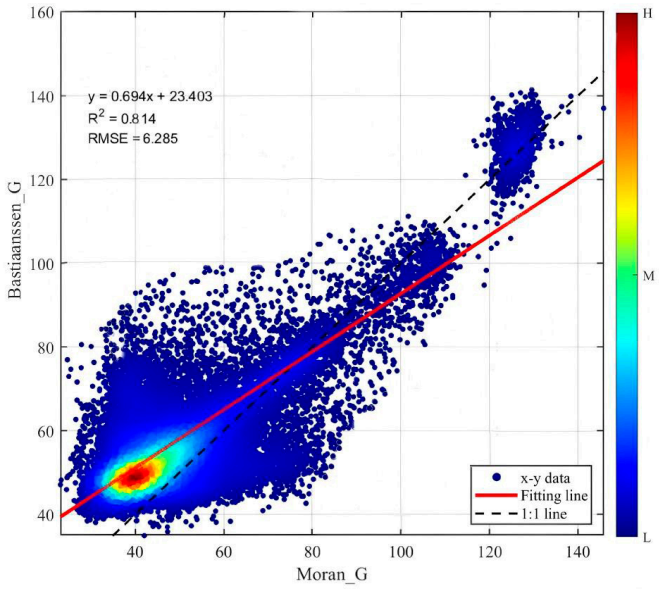


Figure 10. Comparison of soil heat flux (G) estimates from the Bastiaanssen and Moran models for model selection based on the 11:30 UAV image.

3.2. New Similarity Function Fitting and Accuracy Validation

To obtain the similarity function $f_T(\xi)$ of the temperature structure constant (C_T^2) in the near-surface layer of the study area, a near-surface meteorological observation system was established in September 2024, followed by continuous observations. The September observations were used to fit $f_T(\xi)$ for the study area. The quantities u_*, T_*, and ξ were obtained from the measured data using Equations (2)–(4). Subsequently, $f_T(\xi)$ was analyzed in combination with Equation (1), as illustrated in Figure 10. In the figure, the black circles represent the values of $f_T(\xi)$ derived from the field measurements. The curve fitting was conducted within the stability range of $-3 < \xi < 1$. Following the empirical formulations of similarity functions established by previous studies under both stable and unstable conditions, the experimental data were fitted using the same functional forms: $f_T(\xi) = \mathrm{a}(1 - b\xi)^{-2/3}$.

Based on the scatter distribution of $f_T(\xi)$ with respect to ξ, as shown in Figure 11, a near-surface similarity function was fitted for the mixed rural farmland–grassland terrain in Shouxian, as expressed in Equation (22).

$$f_T(\xi) = \begin{cases} 0.31, \xi < -1 \\ 3.94(1 - 44.99\xi)^{-2/3}, -1 \le \xi < 0 \\ 3.82(1 + 44.58\xi)^{-2/3}, 0 \le \xi < 1 \end{cases} \quad (22)$$

Under unstable conditions ($\xi < 0$), the value of the similarity function decreases gradually as atmospheric instability increases. When the instability becomes sufficiently strong ($\xi < -1$), corresponding to a highly unstable atmospheric state, the measured becomes nearly independent of ξ and tends to approach a constant value. Therefore, in this study, the behavior of ξ under unstable conditions is fitted separately for the intervals $\xi < -1$ and $-1 \le \xi < 0$. In contrast, under stable conditions ($\xi > 0$), the classical 2/3 power-law relationship proposed by the W73 model is not satisfied. This discrepancy may be attributed to the local-equilibrium assumption in similarity theory, which may not be valid under stable stratification, where turbulent kinetic energy cannot be sufficiently maintained. In addition, many field observations have reported significant deviations between measured temperature structure constants and theoretical predictions under stable conditions, especially in strongly stable regimes, where the 2/3 scaling is no longer

applicable. It can be seen that under unstable conditions ($\xi < 0$), $f_T(\xi)$ decreases with the increase in instability. Under neutral conditions ($\xi \to 0$), a significantly larger value appears, and under stable conditions ($\xi > 0$), $f_T(\xi)$ decreases with the increase in stability.

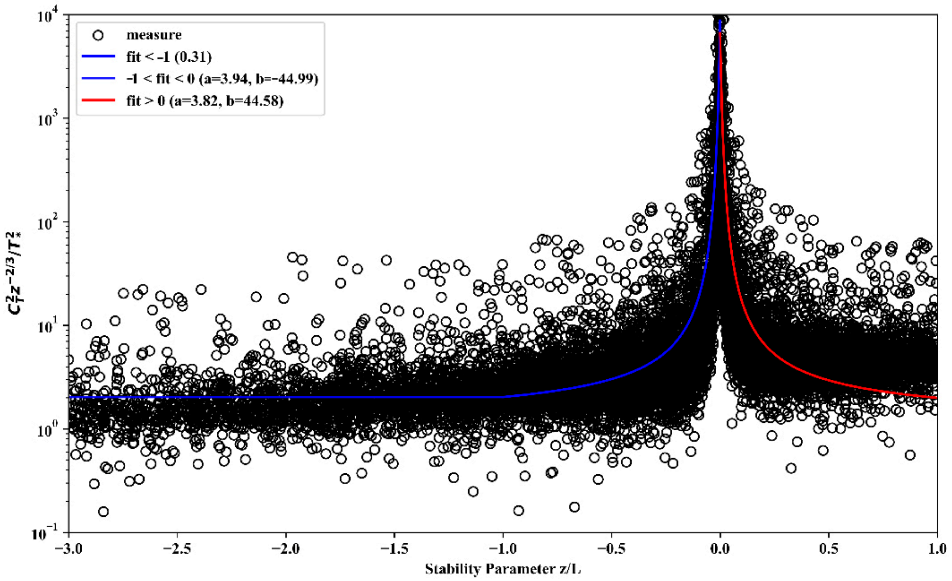


Figure 11. Relationship between the temperature similarity function and the stability parameter.

In this study, the local similarity function $f_T(\xi)$ was fitted exclusively using near-surface observations collected in September 2024. The fitted $f_T(\xi)$ and the conventional W73 model were then applied independently to the October 2024 observations to estimate C_n^2, and the resulting estimates were validated against simultaneous in situ measurements of temperature fluctuations. Thus, the October observations used for validation were not involved in fitting the local similarity function.

The temperature structure constant C_T^2 is obtained from Equations (1)–(5), and a simple correlation exists between the refractive index structure constant C_n^2 and C_T^2 [35]:

$$C_n^2 = \left(79 \times 10^{-6} \frac{P}{T^2}\right)^2 C_T^2 \tag{23}$$

In the equation, P is the atmospheric pressure (hPa) and T is the absolute air temperature (K). Based on the above derivation, a new model for estimating C_n^2 in the study area can be established.

Combining Equations (1), (5), (6) and (21), the relationships for estimating C_T^2 using the W73 model and the new model fitted in this study can be obtained, respectively:

$$\frac{C_T^2 z^{2/3} \mu_*^2 \rho C_P}{H} = \begin{cases} 4.7(1-7\xi)^{-2/3}, x < 0 \\ 4.9\left(1+2.4\xi^{2/3}\right), x \geq 0 \end{cases} \tag{24}$$

$$\frac{C_T^2 z^{2/3} \mu_*^2 \rho C_P}{H} = \begin{cases} 0.31, \xi < -1 \\ 3.94(1-44.99\xi)^{-2/3}, -1 \leq \xi \leq 0 \\ 3.82(1+44.58\xi)^{-2/3}, \xi > 0 \end{cases} \tag{25}$$

The estimated C_T^2 is then substituted into Equation (23) to obtain the C_n^2 values estimated from the UAV remote sensing data combined with the W73 model and the newly fitted model. This yields the two-dimensional spatial distribution of C_n^2 across the study area.

Figure 12 compares the estimated C_n^2 using the conventional W73 function and the newly fitted function. The horizontal axis represents the C_n^2 values measured by the micro-thermometer, while the vertical axis represents the model-estimated C_n^2 values.

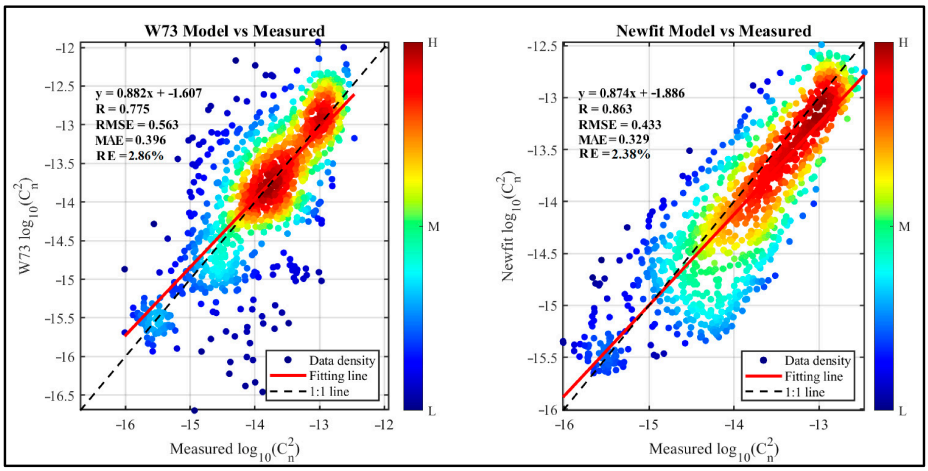


Figure 12. Comparison between measured C_n^2 and estimates derived from the W73 model and the newly fitted similarity function. (**a**) The comparison of the results estimated by the conventional W73 model and (**b**) the results estimated by the newly fitted function.

3.3. UAV-Based Estimation and Accuracy Validation of Refractive Index Structure Constant

The fitted similarity function, combined with UAV−derived estimates of sensible heat flux (H) and near-surface friction velocity (u_*), was used to derive the two-dimensional spatial distribution of $\log_{10}(C_n^2)$ in the study area, as shown in Figure 13.

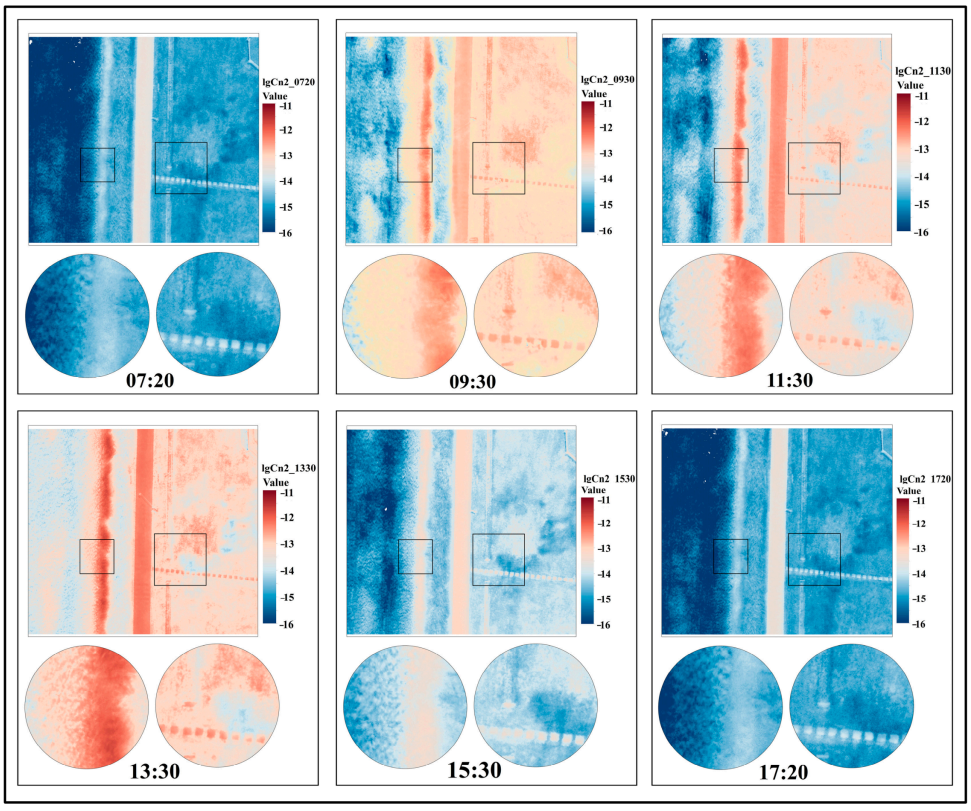


Figure 13. Spatial distribution of atmospheric refractive index structure constant (taking the logarithmic result).

From the perspective of spatial distribution, areas with dense vegetation cover generally exhibited lower C_n^2 values. In these areas, vegetation released water vapor into the atmosphere through transpiration, producing a local cooling effect. This weakened temperature fluctuations in the surrounding air, suppressed atmospheric turbulence, and produced a turbulence-damping effect. In contrast, bare surfaces with low vegetation cover usually had higher surface temperatures and stronger wind speeds, which enhanced convective motion and turbulence, resulting in higher C_n^2 values. Therefore, at the same time, C_n^2 values in high-vegetation-cover areas were generally lower than those in low-vegetation-cover areas. From a temporal perspective, C_n^2 generally increased and then decreased during the day. It reached its maximum around noon and decreased rapidly toward sunset in the afternoon. The daily variation rate was faster in non-vegetated areas than in vegetated areas.

In the estimation of C_n^2 using UAV data in combination with the similarity function, sensible heat flux serves as a crucial input parameter. Nevertheless, the sensible heat flux retrieved from UAV observations based on the semi-empirical triangle method is inevitably subject to uncertainties. To quantify the influence of such uncertainties on near-surface C_n^2 estimation, the sensible heat flux directly measured by a three-dimensional ultrasonic anemometer was additionally substituted into the similarity function to estimate C_n^2. The derived C_n^2 values were subsequently compared with the in situ measurements from micro-thermometer through correlation analysis.

Figure 14a shows that the scatter points between the UAV-derived C_n^2 estimates and the measured values were relatively concentrated, although a few outliers remained. The correlation coefficient (r), coefficient of determination (R^2), and logarithmic root-mean-square error ($RMSE$) were 0.85, 0.72, RMSE was 0.44, with a MAE of 0.34 and an RE of 2.51%, respectively. These results indicate a strong positive correlation between the UAV-derived estimates and the measured values, suggesting that the proposed method can effectively estimate the two-dimensional spatial distribution of C_n^2 over heterogeneous land surfaces. Figure 14b presents the scatter distribution between the C_n^2 estimates obtained by combining the similarity function with sensible heat flux measured by the three-dimensional sonic anemometer and the measurements from the micro-thermometers. Compared with Figure 14b, the scatter points exhibit a higher degree of clustering, with an r of 0.91, an R^2 of 0.82, an $RMSE$ of 0.29, a MAE of 0.22 and an RE of 1.63%.

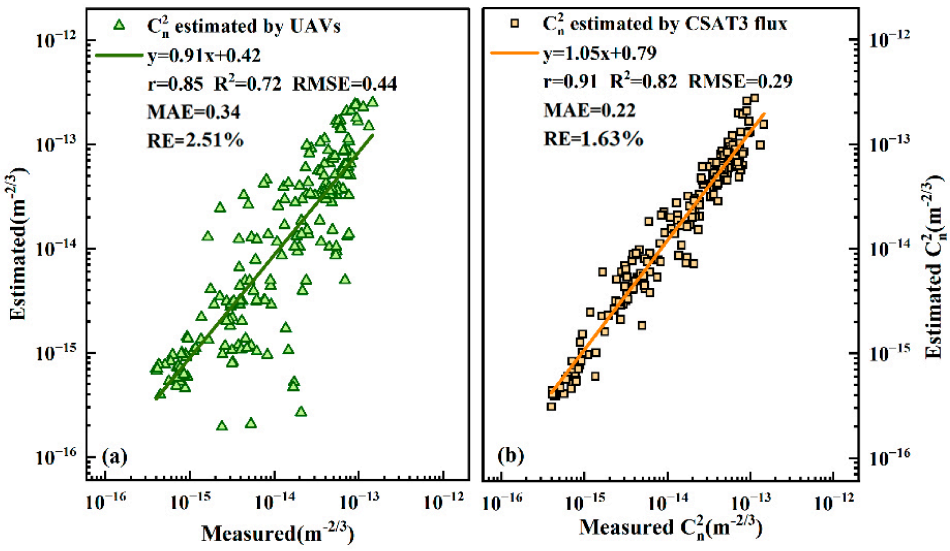


Figure 14. Correlation between measured and estimated $\log_{10}(C_n^2)$ values based on sensible heat fluxes from two data sources.

The comparison indicates that the UAV-derived sensible heat flux is subject to certain estimation uncertainties, which can propagate into the subsequent C_n^2 estimation. Although the UAV-based estimates showed lower agreement with the measurements than those derived using CSAT3B-based sensible heat flux, they still reproduced the main spatial and diurnal variation patterns of C_n^2. Therefore, the proposed UAV framework should be regarded primarily as a complementary approach to conventional point-based measurements, rather than as a replacement for them, with its principal advantage lying in its ability to provide spatially distributed turbulence information over heterogeneous land surfaces.

Figure 15 presents the diurnal variation in C_n^2 derived from the measured data, UAV system, and CSAT3B sonic anemometer. Overall, the three curves show a consistent temporal pattern, with lower values in the early morning and late afternoon and higher values around midday. From 07:00 to 12:00, $\log_{10}(C_n^2)$ increased gradually as solar radiation intensified and surface heating enhanced buoyancy-driven turbulence. Around midday, the atmospheric turbulence reached its strongest level.

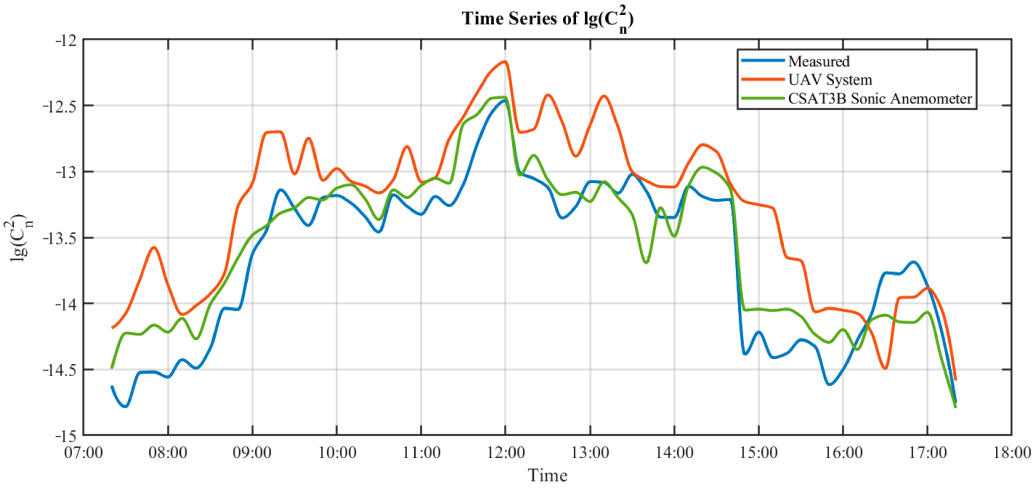


Figure 15. Comparison of diurnal variations in measured $\log_{10}(C_n^2)$ values and estimates derived from the UAV system and CSAT3B sonic anemometer.

The UAV-derived estimates generally reproduced the measured trend but tended to be slightly higher, especially during periods of strong surface heating. The CSAT3B sonic anemometer-based estimates were closer to the measured values and showed better consistency in the timing of the peak. After approximately 14:30, all three curves decreased rapidly, indicating the weakening of atmospheric turbulence as solar radiation and surface sensible heat flux declined. During this period, the atmospheric boundary layer gradually shifted from an unstable state toward a neutral or stable state, thereby suppressing turbulence development. A difference was observed in the peak duration among the three datasets. The UAV-derived $\log_{10}(C_n^2)$ reached its peak around 12:00 and then began to decline, whereas the measured and sonic anemometer-based values remained relatively high until approximately 13:30–14:00. This discrepancy may be attributed to the fact that the UAV-based method primarily relies on surface temperature, which responds more rapidly to changes in solar radiation than atmospheric temperature and wind speed. Despite these differences, the UAV-based method effectively captured the main diurnal variation of $\log_{10}(C_n^2)$, demonstrating its potential for estimating optical turbulence at the planar scale.

Statistical analysis of the pixel values of $\log_{10}(C_n^2)$ on the two-dimensional spatial distribution was conducted to identify the spatial variation patterns of optical turbulence. Based on the statistical distribution of pixel values, the study area could be classified into regions of strong ($-12 \sim -13$), moderate ($-13 \sim -15$), and weak ($-15 \sim -17$)

turbulence. This approach further quantified the spatial heterogeneity of turbulence and provided a more detailed understanding of how different surface types influenced the spatial distribution of C_n^2.

Figure 16 shows the percentage distributions and cumulative percentage curves of $\log_{10}(C_n^2)$ pixel values during representative periods within the study area, derived from Figure 13. Panels (a)–(f) present the statistical results for different time intervals. The histograms indicate that the center of the pixel-value distribution shifted over time and generally followed a normal distribution, which is consistent with the pronounced diurnal variation in atmospheric turbulence intensity. At 07:20, the $\log_{10}(C_n^2)$ pixel values were mainly concentrated in the middle-to-low range, with a peak around −14.0. At 09:30, the overall distribution shifted toward higher values, with the peak occurring around −13.2. At 10:30, the peak further shifted to approximately −12.8, indicating a significant enhancement of optical turbulence intensity around midday. At 13:30, the peak remained near −12.8, while the maximum value increased to −12.2, suggesting that turbulence reached its afternoon maximum due to the cumulative effects of surface heating. At 15:30, the $\log_{10}(C_n^2)$ pixel values began to shift toward lower values, with the peak around −13.8. After 17:30, the distribution gradually returned to lower-value ranges, with the peak again occurring around −14.2.

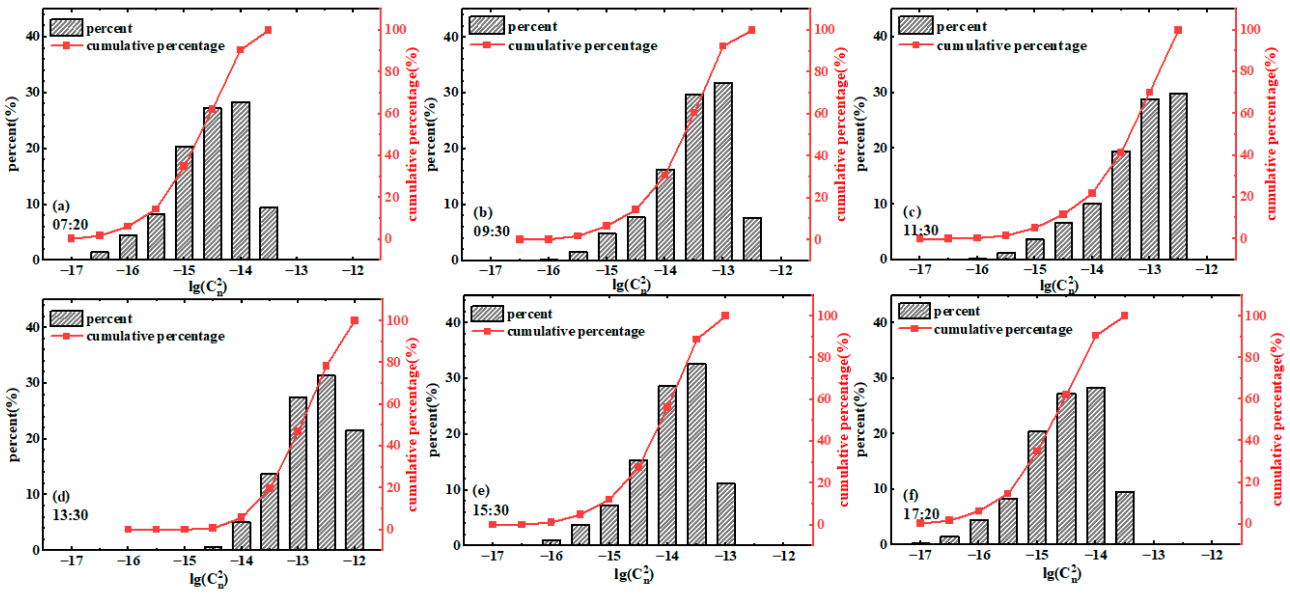


Figure 16. Statistical distributions and cumulative percentage curves of $\log_{10}(C_n^2)$ pixel values at representative times. (**a**) 07:20; (**b**) 09:30; (**c**) 11:30; (**d**) 13:30; (**e**) 15:30; and (**f**) 17:20.

The red cumulative percentage curves during periods of strong turbulence, particularly from 11:30 to 13:30, were noticeably shifted toward higher values, indicating a larger proportion of high $\log_{10}(C_n^2)$ pixels. In contrast, during weak turbulence periods, such as 07:20 and 17:20, the cumulative curves were concentrated in the lower-value range, reflecting weaker optical turbulence. Overall, the statistical analysis of $\log_{10}(C_n^2)$ pixel values provides quantitative evidence for characterizing the spatiotemporal evolution of turbulence and supports further investigation into the relationship between surface characteristics and turbulence intensity.

4. Conclusions

In this study, a UAV-based system suitable for routine meteorological parameter observation and atmospheric optical turbulence intensity estimation was developed. Using

high-resolution flight survey data collected by the UAV system, combined with a semi-empirical triangle method and Monin–Obukhov similarity functions, we estimated the C_n^2 over a mixed farmland and grassland landscape in the rural area of Shouxian, Anhui Province, China. Based on this approach, two-dimensional spatial distributions of C_n^2 was obtained, thereby addressing the challenge of estimating optical turbulence at the "surface" or "plane" scale. This provides a new methodological framework for high-resolution spatial estimation of atmospheric optical turbulence. Compared with conventional point-based or directly transferred empirical approaches, the proposed framework combines high-resolution UAV observations, a semi-empirical triangle method, and a locally fitted Monin–Obukhov similarity function to achieve two-dimensional optical turbulence estimation over heterogeneous farmland–grassland surfaces. This framework not only extends turbulence estimation from the point to the surface scale but also improves the adaptability of the similarity relationship to heterogeneous land surfaces.

According to Monin–Obukhov similarity theory (MOST) in the atmospheric surface layer, the prediction accuracy of C_n^2 largely depends on the functional relationship between the temperature structure constant (C_T^2) and the atmospheric stability parameter ($f_T(\xi)$). While numerous similarity functions have been established for marine or homogeneous environments, their applicability to heterogeneous land surfaces remains limited. To improve the estimation accuracy of near-surface atmospheric optical turbulence intensity in the study area, this study re-fitted a $f_T(\xi)$ suitable for local farmland–grassland mixed surfaces. The performance of the fitted $f_T(\xi)$ was systematically evaluated by comparison with the conventional W73 model, using measured values as the validation benchmark. Statistical analysis revealed that although the W73 model exhibited an r correlation coefficient of 0.775 with the measured data, it showed relatively large estimation uncertainties, particularly under enhanced turbulence conditions. In contrast, the new fitted $f_T(\xi)$ demonstrated superior performance, with the estimated values more closely distributed along the Y = X reference line and showing smaller deviations from the measured values. The improved model achieved an r of 0.863. In addition, $RMSE_{\log}$ was reduced from 0.563 for the W73 model to 0.433 for the new fitted model. These improvements in both correlation strength and error reduction indicate that the refined similarity function provides more reliable and accurate estimates of atmospheric optical turbulence intensity under varying turbulence conditions.

By driving the new fitted $f_T(\xi)$ with UAV-derived H, a two-dimensional spatial distribution of C_n^2 with an ultra-high spatial resolution of 0.045 m was generated. To validate these spatial estimates, the pixel values across the study area were spatially averaged and compared with point-based in situ measurements. The validation yielded an r of 0.85 and an $RMSE_{\log}$ of 0.44, confirming the high fidelity of the UAV-based estimates and proving that high-resolution UAV data can effectively retrieve spatial distributions of C_n^2. Pixel-level statistical analysis revealed that $\log_{10}(C_n^2)$ exhibits a distinct diurnal pattern characterized by "peaking at noon and remaining low in the early morning and evening." Spatially, areas with higher vegetation cover systematically exhibited lower C_n^2 values, a pattern that is highly consistent with the spatial heterogeneity of H over varying vegetative surfaces.

5. Discussion

The results demonstrate the potential of an integrated framework that combines high-resolution UAV remote sensing, surface energy-balance estimation, and a locally adapted atmospheric similarity relationship for extending C_n^2 estimation from the conventional point scale to the two-dimensional surface scale.

The methodological contribution of this study lies not simply in the use of UAV observations, but in establishing an integrated framework that combines high-resolution surface remote sensing, surface energy-balance estimation, and a locally adapted atmospheric similarity relationship for two-dimensional estimation of the atmospheric refractive index structure parameter (C_n^2). Compared with conventional approaches that rely on discrete point observations or directly apply general similarity functions, the proposed framework provides spatially continuous C_n^2 information at high resolution while accounting for the heterogeneity of farmland–grassland surfaces. In particular, the locally fitted similarity function showed improved performance compared with the conventional W73 model, demonstrating the benefit of adapting the C_n^2-related similarity relationship to local surface conditions. By linking UAV-derived surface characteristics with surface energy fluxes and atmospheric similarity theory, the proposed framework extends C_n^2 estimation from the traditional point scale toward the two-dimensional surface scale and provides complementary spatial information for applications requiring high-resolution characterization of atmospheric optical turbulence. Meanwhile, the comparison between the UAV-based estimates and the CSAT3B in situ measurements helps clarify the uncertainty introduced by remotely sensed sensible heat flux into the C_n^2 estimation process. When the same similarity function was applied, the UAV-based estimates showed lower accuracy than those derived using sensible heat flux measured by the CSAT3B. Nevertheless, the UAV-based estimates still exhibited a strong correlation with the in situ measurements ($r = 0.85$), indicating that the method was able to capture the overall variability of atmospheric optical turbulence despite the additional uncertainties associated with remotely sensed sensible heat flux. The lower agreement with the in situ measurements therefore primarily reflects the uncertainty propagated from the remote sensing-based sensible heat flux estimation rather than a limitation of the UAV framework in resolving spatial variability. Accordingly, the objective of the UAV-based approach is not to replace high-precision point-scale measurements, but rather to extend their information spatially across heterogeneous land surfaces. Ground-based measurements provide reliable point-scale characterization, whereas UAV observations provide spatially continuous information, enabling the fine-scale heterogeneity of atmospheric optical turbulence to be resolved across different surface types.

Nevertheless, several limitations remain in the present study. First, the UAV system developed here was equipped only with temperature and humidity sensors for routine meteorological observations and did not include a wind speed sensor. This limitation is important because the estimation of C_n^2 is closely related to atmospheric wind conditions, and the friction velocity (u_*) derived from wind observations is a key variable in the estimation of the temperature structure parameter and subsequently C_n^2. Due to practical constraints during the initial field experiment, the UAV-based system was not equipped with an ultrasonic anemometer. Therefore, C_n^2 was calculated using three-dimensional wind speed fluctuations measured by a near-surface 3D ultrasonic anemometer and subsequently incorporated into the relevant similarity models. Although the comparison between the estimated and measured C_n^2 showed satisfactory agreement, the use of near-surface wind observations introduces a degree of dependence on ground-based meteorological measurements and consequently limits the observational independence of the UAV system. Second, the current framework involves several intermediate parameterization and estimation steps, including sensible heat flux estimation, the determination of extreme points in the triangle space, and soil heat flux parameterization. Although the UAV-derived LST and NDVI were calibrated and quality-controlled during data preprocessing, the uncertainties associated with triangle space extreme value determination and soil heat flux parameterization may still propagate into the final C_n^2 estimation. In addition, the individual contributions of these error sources have not yet been completely separated and quantitatively assessed.

Further sensitivity experiments are therefore needed to clarify their relative contributions and improve the uncertainty characterization of the proposed framework. Third, the field experiments in this study were conducted under specific surface and atmospheric conditions, and the UAV observations were performed at a fixed flight height. Therefore, the applicability of the proposed method under different atmospheric stability conditions, surface types, wind regimes, and observation heights requires further verification. In particular, the transferability of the empirically fitted similarity functions to different sites and atmospheric conditions should be evaluated using more extensive multi-seasonal and multi-site observations.

In future work, where experimental conditions permit, an ultrasonic anemometer will be integrated into the UAV platform to directly measure wind speed and three-dimensional wind fluctuations. Combined with near-surface similarity theory and iterative calculation, this will enable more independent retrieval of turbulence characteristics and reduce the reliance on ground-based wind observations for UAV-based C_n^2 estimation. Meanwhile, additional controlled sensitivity experiments will be conducted to quantify error propagation and evaluate the robustness of the parameterization schemes. Multi-height and multi-site observations will also be implemented under diverse atmospheric and surface conditions to further assess the transferability and generalizability of the proposed framework and improve its uncertainty characterization.

Author Contributions: C.L.: methodology, software, formal analysis, writing—original draft preparation. S.D.: funding acquisition, investigation. X.L.: investigation, data curation. T.L.: funding acquisition, writing—review and editing, formal analysis, conceptualization. All authors have read and agreed to the published version of the manuscript.

Funding: This research was funded by The Strategic Priority Research Program of Chinese Academy of Sciences (XDA17010104); the General Program of the National Natural Science Foundation of China (41875041); and the Natural Science Foundation for Distinguished Young Scholars of Anhui Province (2008085J19).

Data Availability Statement: The data underlying this article cannot be shared publicly due to the confidentiality requirements of the project in the study.

Acknowledgments: The authors sincerely acknowledge the editors' and reviewers' efforts in improving the manuscript.

Conflicts of Interest: The authors declare no conflicts of interest.

Abbreviations

Definitions and Units of Variables and Parameters Used in Equations (1)–(21).

Symbol	Physical meaning	Unit	Eq.
C_T^2	Temperature structure parameter	$K^2m^{-2/3}$	(1)
C_n^2	Refractive index structure parameter	$m^{-2/3}$	(23)
$f_T(\xi)$	Dimensionless temperature similarity function	-	(1), (5), (22)
ξ	Atmospheric stability parameter	-	(1), (2), (5)
L	Monin–Obukhov length	m	(2)
u_*	Friction velocity	ms^{-1}	(1)–(4)
T_*	Temperature scale	K	(1), (2), (4)
T'	Temperature fluctuation	K	(2)
w'	Fluctuation of the vertical wind-speed	ms^{-1}	(2), (3)
H	Sensible heat flux	Wm^{-2}	(6), (9)
LE	Latent heat flux	Wm^{-2}	(7), (8)
R_n	Net radiation	Wm^{-2}	(8), (9), (13), (14)
G	Soil heat flux	Wm^{-2}	(8), (9), (13), (14)

LST	Land surface temperature	°C	(10), (13), (16)
$NDVI$	Normalized difference vegetation index	-	(13), (14)
$NDRE$	Normalized difference red edge index	-	(11), (15)
ϕ	Priestley–Taylor coefficient	-	(9)–(12)
P	Atmospheric pressure	hPa	(19)
T	Absolute air temperature	K	(19)
r	Pearson correlation coefficient	-	(17)
R^2	Coefficient of determination	-	(19)
$RMSE$	Root mean square error	Variable-dependent	(18)
MAE	Mean absolute error	Variable-dependent	(20)
RE	Relative error	%	(21)

References

1. Ata, Y.; Baykal, Y.; Gökçe, M.C. Average Channel Capacity in Anisotropic Atmospheric Non-Kolmogorov Turbulent Medium. *Opt. Commun.* **2019**, *451*, 129–135. [CrossRef]
2. Alterman, M.; Schechner, Y.Y.; Vo, M.; Narasimhan, S.G. Passive Tomography of Turbulence Strength. In *Computer Vision—ECCV 2014*; Fleet, D., Pajdla, T., Schiele, B., Tuytelaars, T., Eds.; Lecture Notes in Computer Science; Springer International Publishing: Cham, Switzerland, 2014; Volume 8692, pp. 47–60.
3. Bendersky, S.; Kopeika, N.S.; Blaunstein, N. Atmospheric Optical Turbulence over Land in Middle East Coastal Environments: Prediction Modeling and Measurements. *Appl. Opt. AO* **2004**, *43*, 4070–4079. [CrossRef] [PubMed]
4. Liu, Y.; Luo, T.; Yang, K.; Zhang, H.; Zhu, L.; Shao, S.; Cui, S.; Li, X.; Weng, N. Estimation of Atmospheric Boundary Layer Turbulence Parameters over the South China Sea Based on Multi-Source Data. *Remote Sens.* **2025**, *17*, 1929. [CrossRef]
5. Saha, R.K.; Salcin, E.; Kim, J.; Smith, J.; Jayasuriya, S. Turbulence Strength Cn2 Estimation from Video Using Physics-Based Deep Learning. *Opt. Express OE* **2022**, *30*, 40854–40870. [CrossRef] [PubMed]
6. Pierzyna, M.; Hartogensis, O.; Basu, S.; Saathof, R. Intercomparison of Flux-, Gradient-, and Variance-Based Optical Turbulence (Cn2) Parameterizations. *Appl. Opt.* **2024**, *63*, E107–E119. [CrossRef] [PubMed]
7. Li, Z.; Pu, O.; Pan, Y.; Huang, B.; Zhao, Z.; Wu, H. A Study on Measuring the Wind Field in the Air Using a Multi-Rotor UAV Mounted with an Anemometer. *Bound. Layer Meteorol.* **2023**, *188*, 1–27. [CrossRef]
8. Bulusu, M.; Ellsasser, F.J.; Hendrayanto; Holscher, D.; Roll, A. Fine-Scale Spatial Variation of Evapotranspiration across Tropical Land-Cover Mosaics Revealed by UAV Thermography. *Hydrol. Process.* **2026**, *40*, e70611. [CrossRef]
9. Mourgelas, C.; Micha, E.; Chatzistavrakis, E.; Voyiatzis, I. Classification of Unmanned Aerial Vehicles in Meteorology: A Survey. *Environ. Sci. Proc.* **2023**, *26*, 135. [CrossRef]
10. Alaoui-Sosse, S.; Durand, P.; Medina, P.; Pastor, P.; Lothon, M.; Cernov, I. OVLI-TA: An Unmanned Aerial System for Measuring Profiles and Turbulence in the Atmospheric Boundary Layer. *Sensors* **2019**, *19*, 581. [CrossRef] [PubMed]
11. Wang, F.; Zhang, K.; Sun, G.; Liu, Q.; Li, X.; Luo, T. Study of the Cn2 Model through the New Dimensionless Temperature Structure Function near the Sea Surface in the South China Sea. *Remote Sens.* **2023**, *15*, 631. [CrossRef]
12. Michaels, T.I.; Rafkin, S.C.R. Large-Eddy Simulation of Atmospheric Convection on Mars. *Q. J. R. Meteorol. Soc.* **2004**, *130*, 1251–1274. [CrossRef]
13. Wyngaard, J.C. *Turbulence in the Atmosphere*; Cambridge University Press: Cambridge, UK, 2010.
14. Li, B.; Jiang, J.; Chen, Y.; Huang, Z. Deep Learning-Based Deflection Angle Regression Network for Measurement of the Atmospheric Refractive Index Structure Constant. *Appl. Opt.* **2026**, *65*, 719–728. [CrossRef] [PubMed]
15. Mu, Y.; Zhou, L.; Shao, S.; Wang, Z.; Tang, P.; Hu, Z.; Ye, L. Atmospheric Turbulence Intensity Image Acquisition Method Based on Convolutional Neural Network. *Remote Sens.* **2025**, *17*, 103. [CrossRef]
16. Zhang, X.; Luo, B.; Liu, Y.; Li, J.; Liang, T.; Hong, J.; Li, C. Development of UAV-Based System for Simultaneous Wind and Particle Measurements in the Atmospheric Boundary Layer. *Exp. Fluids* **2025**, *66*, 139. [CrossRef]
17. Saboohi, Z.; Moradi, A.; Hosseini, S.E.; Karimi, N. Experimental Investigation of Atmospheric Boundary Layer Using Unmanned Aerial System Equipped with Novel Measurement System. *Meteorol. Atmos. Phys.* **2025**, *137*, 13–21. [CrossRef]
18. Wang, Y.; Jin, D.; Chen, J.; Bai, X. Revelation of Hidden 2D Atmospheric Turbulence Strength Fields from Turbulence Effects in Infrared Imaging. *Nat. Comput. Sci.* **2023**, *3*, 687–699. [CrossRef] [PubMed]
19. Zhou, Q.; Su, Q.; Wei, X.; Mao, W.; Ren, Y.; Chen, Y.; Bi, J.; Zhao, M.; Tsukada, M. CLIFF: A Multi-Modal Remote Sensing Model for Geological Hazard Monitoring Based on Bitemporal UAV Images. *Remote Sens.* **2026**, *18*, 2432. [CrossRef]
20. Yang, Q.; Wu, X.; Luo, T.; Qing, C.; Yuan, R.; Su, C.; Xu, C.; Wu, Y.; Ma, X.; Wang, Z. Forecasting Surface-Layer Optical Turbulence above the Tibetan Plateau Using the WRF Model. *Opt. Laser Technol.* **2022**, *153*, 108217. [CrossRef]

21. Liu, C.; Deng, S.; Yang, K.; Ma, X.; Zhang, K.; Li, X.; Luo, T. The Unmanned Aerial Vehicle-Based Estimation of Turbulent Heat Fluxes in the Sub-Surface of Urban Forests Using an Improved Semi-Empirical Triangle Method. *Remote Sens.* **2024**, *16*, 2830. [CrossRef]
22. Wyngaard, J.C.; Izumi, Y.; Collins, S.A. Behavior of the Refractive-Index-Structure Parameter near the Ground*. *J. Opt. Soc. Am. JOSA* **1971**, *61*, 1646–1650. [CrossRef]
23. Shikhovtsev, A.; Kovadlo, P.; Lukin, V.; Nosov, V.; Kiselev, A.; Kolobov, D.; Kopylov, E.; Shikhovtsev, M.; Avdeev, F. Statistics of the Optical Turbulence from the Micrometeorological Measurements at the Baykal Astrophysical Observatory Site. *Atmosphere* **2019**, *10*, 661. [CrossRef]
24. Lee, T.R.; Meyers, T.P. New Parameterizations of Turbulence Statistics for the Atmospheric Surface Layer. *Mon. Weather Rev.* **2023**, *151*, 85–103. [CrossRef]
25. Lei, K.; Cheng, F.; Liu, T.; Liu, R.; Zhang, A. Multi-Factor Air-Sea Heat Exchange Study on the Thermal Discharge Diffusion at Coastal Nuclear Power Plants: Sensitivity and Contribution Analysis. *Water* **2026**, *18*, 758. [CrossRef]
26. Petropoulos, G.P.; Hristopulos, D. Retrievals of Key Biophysical Parameters at Mesoscale from the Ts/VI Scatterplot Domain. *Geocarto Int.* **2022**, *37*, 2385–2405. [CrossRef]
27. Tang, R.; Li, Z.-L. Evaluation of Two End-Member-Based Models for Regional Land Surface Evapotranspiration Estimation from MODIS Data. *Agric. For. Meteorol.* **2015**, *202*, 69–82. [CrossRef]
28. Asharaf, S.; Crespo, J.A.; Posselt, D.J.; Bourassa, M.A. Advancing CYGNSS-Derived Ocean Surface Heat Fluxes. *Remote Sens.* **2026**, *18*, 694. [CrossRef]
29. Hotovy, O.; Jenicek, M. The Impact of Changing Subcanopy Radiation on Snowmelt in a Disturbed Coniferous Forest. *Hydrol. Process.* **2020**, *34*, 5298–5314. [CrossRef]
30. de Morais Danelichen, V.H.; Biudes, M.S.; Souza, M.C.; Machado, N.G.; da Silva, B.B.; Nogueira, J.d.S. Estimation of Soil Heat Flux in a Neotropical Wetland Region Using Remote Sensing Techniques. *Rev. Bras. Meteorol.* **2014**, *29*, 469–482. [CrossRef]
31. Sandholt, I.; Rasmussen, K.; Andersen, J. A Simple Interpretation of the Surface Temperature/Vegetation Index Space for Assessment of Surface Moisture Status. *Remote Sens. Environ.* **2002**, *79*, 213–224. [CrossRef]
32. Marty, C.; Khare, S.; Rossi, S.; Lafond, J.; Boivin, M.; Pare, M.C. Detection of Management Practices and Cropping Phases in Wild Lowbush Blueberry Fields Using Multispectral UAV Data. *Can. J. Remote Sens.* **2022**, *48*, 469–480. [CrossRef]
33. Marzahn, P.; Flade, L.; Sanchez, A. Spatial Estimation of the Latent Heat Flux in a Tropical Dry Forest by Using Unmanned Aerial Vehicles. *Forests* **2020**, *11*, 604. [CrossRef]
34. Su, B.; Wang, C.; Hang, R.; Chen, S. Estimation of Spatial Distribution of Field-Scale Evapotranspiration. *Trans. Chin. Soc. Agric. Mach.* **2020**, *51*, 156–163.
35. Yang, K.; Luo, T.; Li, X.; Cui, S.; Liu, Q.; Zhang, K. Correction Method for a Shipborne Ultrasonic Anemometer in Measuring the Refractive Index Structure Constant in a Marine Environment. *Appl. Opt.* **2024**, *63*, 5802. [CrossRef]

Disclaimer/Publisher's Note: The statements, opinions and data contained in all publications are solely those of the individual author(s) and contributor(s) and not of MDPI and/or the editor(s). MDPI and/or the editor(s) disclaim responsibility for any injury to people or property resulting from any ideas, methods, instructions or products referred to in the content.